Front. Mater. Sci. 2021, 15(4): 577–588
https://doi.org/10.1007/s11706-021-0579-z

RESEARCH ARTICLE

Fe-doped $NiCo_2O_4$ hollow hierarchical sphere as an efficient electrocatalyst for oxygen evolution reaction

Wenqing ZHENG[1], Han SUN[1], Xinping LI[1], Shu ZHANG[1], Zhuoxun YIN (✉)[1,2], Wei CHEN (✉)[2], and Yang ZHOU (✉)[3]

1 College of Chemistry and Chemical Engineering, Qiqihar University, Qiqihar 161006, China
2 Heilongjiang Provincial Key Laboratory of Catalytic Synthesis for Fine Chemicals, Qiqihar 161006, China
3 College of Science, Qiqihar University, Qiqihar 161006, China

ABSTRACT: We prepared porous Fe-doped nickel cobaltate (Fe-$NiCo_2O_4$) hollow hierarchical nanospheres through a facile self-templated synthetic strategy. Due to the porous hollow structure and composition, the Fe-$NiCo_2O_4$ presented vastly superior electrocatalytic activity for the oxygen evolution reaction (OER), compared with $NiCo_2O_4$ and the majority of other OER catalysts. With an aim of stimulating a current density of 10 $mA \cdot cm^{-2}$, the Fe-$NiCo_2O_4$ catalyst needs an overpotential of 210 mV, which is on a par with the general properties of commercial IrO_2. In addition, the Fe-$NiCo_2O_4$ catalyst performed stably in long-term testing. The excellent activity and long-term stability showed that such catalysts have great promise for widespread application in the field of water splitting.

KEYWORDS: ion exchange; hierarchical nanostructure; electronic structure transfer; oxygen evolution reaction; water splitting

Contents

Received July 28, 2021; accepted October 19, 2021

E-mails: yzx@qqhru.edu.cn (Z.Y.), chenwei150080@163.com (W.C.), 373133430@qq.com (Y.Z.)

1 Introduction

With the acceleration of global industrialization, dependence on energy has inevitably increased. The rapid growth in fossil fuel consumption and the resulting anthropogenic greenhouse effect have generated great research interest in the development of clean and sustainable energy storage and related conversion technologies [1–2]. The electrochemical hydrogen evolution reaction (HER) and oxygen evolution reaction (OER) are regarded as some of the simplest and most environmentally friendly hydrogen production routes, which make widespread utilization of hydrogen energy possible and thus reduce the existing

dependence on fossil fuels [3–4]. Nevertheless, the efficiency of water electrolysis is limited, in part, by the sluggish anodic OER because of its multi-step proton-coupled electron transfer process. Currently, noble metal-based materials (IrO_2 and RuO_2) are considered to be the best performing OER catalysts, but the high cost and scarce reserves impose severe restrictions on their practical use [5]. Hence, the development of a highly active and low-cost OER catalyst is urgently needed to lower the energy barrier and speed up the water decomposition process.

Recently, the development of first-row transition metal (Fe, Co, Ni, etc.) materials, which are relatively plentiful in the earth's crust, to replace precious metal materials as OER catalysts has attracted huge interest. These materials include transition metal oxides [6–7], hydroxides/hydroxides [8] and other transition metal compounds [9–13]. Nickel cobaltate ($NiCo_2O_4$) is a typical spinel mixed valence metal composite oxide. In its crystal structure, nickel ions occupy the octahedral position, while cobalt ions occupy both octahedral and tetrahedral positions. The presence of solid-state redox pairs of Co^{2+}/Co^{3+} and Ni^{2+}/Ni^{3+} in the structure provides two active sites [14–16]. In particular, $NiCo_2O_4$ has good electrical conductivity compared with single NiO and Co_3O_4. Furthermore, it is shown that $NiCo_2O_4$ is an excellent catalyst for water decomposition, and is more conducive to promoting the performance optimization of its composites. The rich availability in the Earth's crust makes it suitable for large-scale industrial application. However, it is found that the overpotential of $NiCo_2O_4$ catalysts can be higher than 300 mV, which is largely caused by its poor electrical conductivity and small active area. In order to improve the electrocatalytic water splitting activity of $NiCo_2O_4$, modifications of the physical and chemical properties have been investigated and are reported herein.

To gain more active sites, the hollow nanostructure with various hierarchical characteristics has stimulated intense interest in catalyzing OER due to its hollow inside, porosity, and large surface area. Microspheres characterized by their porosity have provoked particular interest; these increase the exposure of active sites to the electrolyte, expediting the diffusion of electrolyte to the active species, and boosting the release of the resulting oxygen bubbles from the catalyst surface. Until now, many nanostructured electrochemical OER catalysts have been investigated. For instance, Co_3O_4/NBGHSs [17], Co-NHCs [18], $NiS_{2(1-x)}Se_{2x}$ [19], β-Mo_2C/C [20], N-doped carbon spheres with hollow interior [21], and C-doped Co/Co_3O_4 [22] have all been applied for catalyzing the OER. Although hollow microsphere electrocatalysts have great superiority in terms of the huge number of active sites, weak intrinsic activity of each catalytic site still imposes restrictions.

In order to strengthen the activity of the catalytic sites, introducing heteroatoms into the catalyst host is an important approach. Ni–Fe and Co–Fe catalysts are the most typical complexes among the hybrid metal-doped catalyst host [23–26]. For example, Friebel et al. discovered that OER activity of $Ni_{1-x}Fe_xOOH$ is 500-fold stronger than that of its pure Ni and Fe parent compounds when it is utilized as an OER catalyst. In addition, they noticed that the real OER active sites were transformed from Ni^{3+} to Fe^{3+} in $Ni_{1-x}Fe_xOOH$ [23]. Burke et al. found that the turnover frequency (TOF) of $Co_{1-x}Fe_x(OOH)$ when $x \approx 0.6$–0.7 is about 100 times higher than that when $x = 0$ [24]. However, developing $NiCo_2O_4$ catalysts features superior OER activity performance and stability is still a huge challenge.

In this study we designed an uncomplicated method to prepare different-valence iron atoms doped-hierarchical nanosheet-based $NiCo_2O_4$ nanospheres. Then, we studied the effects of different-valence iron atoms doping on the OER activities of nanospheres. The electrocatalytic OER activities of iron-doped hierarchical nanosheet-based $NiCo_2O_4$ nanospheres were obtained from polarization curves, from which, we discovered that Fe^{3+}-$NiCo_2O_4$ nanospheres presented the best OER activity, surpassing the majority of OER catalysts reported lately; Fe^{2+} doping also enhanced the electrocatalytic oxygen evolution activity of $NiCo_2O_4$ nanospheres. For instance, to stimulate a current density of 10 $mA \cdot cm^{-2}$, the Fe^{3+}-doped hierarchical nanosheet-based $NiCo_2O_4$ nanospheres electrocatalyst (Fe^{3+}-$NiCo_2O_4$) only needs an overpotential of 210 mV when performing a catalytic operation in OER. Furthermore, Fe^{3+}-$NiCo_2O_4$ showed excellent stability. The outstanding activity and favorable stability demonstrated that Fe^{3+}-$NiCo_2O_4$ has great prospects for widespread application in the field of water splitting.

2 Materials and methods

2.1 Materials

All the reagents used were of the analytical grade and were directly utilized with no purification. $Co(NO_3)_2 \cdot 6H_2O$, $Ni(NO_3)_2 \cdot 6H_2O$, glycerol, isopropanol, and potassium

hydroxide were obtained from Guangfu Fine Chemical Research Institute (Tianjin, China). The commercial IrO_2 catalyst was from Macklin Biochemical Co., Ltd. Carbon paper was purchased from Hesen Electric Co., Ltd. (Shanghai, China). The commercial graphite rod and Ag/AgCl (KCl saturated) electrode were acquired from AIDA Science-Technology Development Co., Ltd. (Tianjin, China). Ultrapure water (>18 MΩ) was used to prepare all the aqueous solutions.

2.2 Synthesis of Fe^{3+}-$NiCo_2O_4$ hollow hierarchical sphere

A total of 2 mmol of $Co(NO_3)_2\cdot 6H_2O$ and $Ni(NO_3)_2\cdot 6H_2O$ with the molar ratio of 1:1 were dissolved in a mixed solution of glycerol of 7 mL and isopropanol of 25 mL, to get a transparent pink solution, which was then moved to a stainless steel autoclave lined with Teflon and kept at a temperature of 180 °C for 6 h. When the autoclave cooled down naturally to room temperature, the precipitate was washed with ethanol several times and then dried in an oven at a temperature of 60 °C. After annealed (500 °C, 10 min), the obtained powders and 50 mg $Fe(NO_3)_3\cdot 6H_2O$ were dissolved in ethanol. The suspension was moved to a Teflon-lined stainless-steel autoclave and stored at a temperature of 160 °C for 4 h. When the autoclave cooled down naturally to room temperature, the precipitate was washed with the distilled water and ethanol several times and then dried in an oven at a temperature of 60 °C.

2.3 Electrochemical measurements

Electrochemical measurements were conducted in a three-electrode system at an electrochemical station (CHI660E, CH Instrument, USA). Three electrodes included the carbon paper which is used as the working electrode (1 cm^2), graphite rod as the counter electrode and Ag/AgCl (KCl saturated) as the reference electrode. The loading mass of the catalysts was around 3.5 $mg\cdot cm^{-2}$ for all the working electrodes. Electrochemical measurements of the catalysts were surveyed in 1 $mol\cdot L^{-1}$ KOH solution through purging the electrolyte with N_2 gas for 30 min. Linear sweep voltammetry (LSV) at a scanning rate of 2 $mV\cdot s^{-1}$ was utilized to get polarization curves. The equation used to calibrate all the measured potentials to reversible hydrogen electrode (RHE) is as follows:

$$E(\mathrm{RHE})/\mathrm{V} = E(\mathrm{Hg/HgO})/\mathrm{V} + 0.098 + 0.059 \times \mathrm{pH} \quad (1)$$

2.4 Features of structure

Scanning electron microscopy (SEM) was performed with the use of a HITACHI SU8000 operating at 15 keV. Transmission electron microscopy (TEM) images were obtained using a FEI Tecnai-F20 transmission electron microscope fitted with a Gatan imaging filter (GIF). A Thermo ESCALAB250 spectrometer was utilized to perform X-ray photoelectron spectroscopy (XPS). X-ray diffraction (XRD) was carried out on a X-Pert Pro diffractometer with Cu Kα radiation (λ = 1.5418 Å). By means of energy dispersive X-ray spectrometry (EDS) and inductively coupled plasma optical emission spectrometry (ICP-OES), metal contents in the catalysts could be detected.

3 Results and discussion

In an attempt to comprehend the formation of porous structures, the doping by various valence state iron ion was performed, and the crystal structures of the catalysts were examined by XRD as is presented in Fig. 1. We discovered no obvious iron-based oxide/hydroxide peaks in the XRD patterns, while all featured peaks belong to $NiCo_2O_4$, suggesting partial substitution of Fe for Ni in nickel hydroxide. The diffraction peaks symbolized by the Miller indices in Fe^{3+}-$NiCo_2O_4$ hollow hierarchical sphere can be indexed to cubic $NiCo_2O_4$ (JCPDS card No. 02-1074, cell parameters: $a = b = c$ = 5.95 Å). A series of typical diffraction peaks were observed at 31.137°, 36.649°, 44.599°, 55.294°, 58.969° and 64.677° for each sample, pointing respectively to (2 2 0), (3 1 1), (4 0 0), (4 2 2), (5 1 1) and (4 4 0) crystal planes of the spinel structure of $NiCo_2O_4$, which indicated the existence of $NiCo_2O_4$. From the XRD diagram, we also find that the diffraction peaks of the Fe^{3+}-$NiCo_2O_4$ hollow hierarchical sphere were weaker than the $NiCo_2O_4$ hollow hierarchical sphere, indicating a decrease in crystallinity of $NiCo_2O_4$. Detailed comparison of the XRD patterns shows that the diffraction peak positions of Fe^{3+}-$NiCo_2O_4$ hollow hierarchical sphere shift toward lower diffraction degrees, which is attribute to the slightly wider distance among the corresponding lattice owing to the Fe incorporation.

Here, the hydrothermal ion exchange for iron doping strategy was performed to synthesize Fe^{3+}-$NiCo_2O_4$ hierarchical hollow spheres with rich edge structure. The synthesis procedure of Fe^{3+}-$NiCo_2O_4$ is shown in Fig. 2(a).

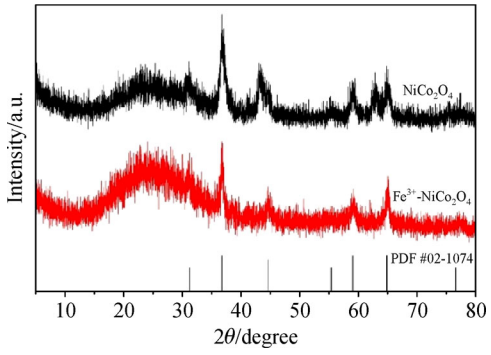

Fig. 1 XRD patterns of $NiCo_2O_4$ and Fe^{3+}-$NiCo_2O_4$.

NiCo solid nanosphere precursors were first prepared using a simple solvothermal method, and then converted into $NiCo_2O_4$ hollow hierarchical spheres by simple annealing in air atmosphere. Finally, after ion exchange etching process, Fe^{3+}-$NiCo_2O_4$ hollow hierarchical sphere were prepared. For comparison experiments, we also prepared Fe^{2+}-$NiCo_2O_4$ by doping with ferrous ion in the same way.

The surface structure of the Fe^{3+}-$NiCo_2O_4$ hierarchical hollow sphere was further characterized by SEM. Figures 2 and S1 show SEM images of the NiCo precursor, Fe^{2+}-$NiCo_2O_4$, Fe^{3+}-$NiCo_2O_4$ and $NiCo_2O_4$. The morphology of the precursor has an obvious change after Fe is added through the ion exchange etching process. Figures 2 (b) and 2(c) show that the NiCo precursor had smoothly spherical shape with a diameter of about 550 nm. Figure S1 shows that the smooth sphere became rough and porous after annealing in air atmosphere. Figure 2(d) indicates a SEM image of Fe^{2+}-$NiCo_2O_4$. The rough and porous nanospheres were further transformed into sea urchin-like nanospheres, composed of many nanospines. Figure 2(e) exhibits that due to ion exchange etching the central part of the sea urchin-shaped nanosphere was hollow. For the Fe^{3+}-$NiCo_2O_4$ nanosphere (Figs. 2(f) and 2(g)), many nanosheets grew almost vertically on the surface of nanospheres, forming a three-dimensional (3D) hierarchical structure. The nanospheres with open ends indicated that the central parts of nanosheet-based Fe^{3+}-$NiCo_2O_4$ nanosphere were hollow (Fig. 2(g)). Determination of the atomic percentage of Fe relative to the total sum of Fe + Ni + Co was through ICP and energy-dispersive X-ray spectroscopy (EDX) (Fig. S2). For the Fe^{3+}-$NiCo_2O_4$ nanosphere, the atom percentage of Fe was about 11.5%, while for the Fe^{2+}-$NiCo_2O_4$ nanosphere, it was about 8.1%. Iron atoms replaced nickel atoms in the Fe^{3+}-$NiCo_2O_4$ nanosphere, while iron atoms replaced cobalt atoms in the Fe^{2+}-$NiCo_2O_4$ nanosphere.

The structure of Fe^{3+}-$NiCo_2O_4$ was further studied by TEM. Figure 3(a) shows that Fe^{3+}-$NiCo_2O_4$ was a hollow sphere with opening, around which a mixed and disordered ultrathin nanosheet structure grew almost vertically, finally looking like the tropical fruit rambutan. In addition, the high-resolution TEM (HRTEM) image of Fe^{3+}-$NiCo_2O_4$ in Fig. 3(a) suggests that the nanosheets were composed of

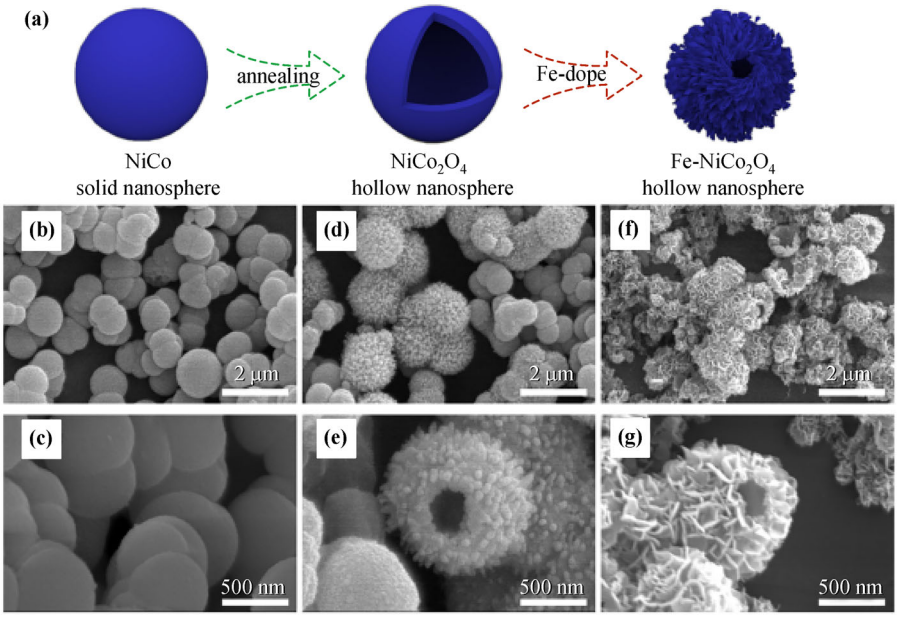

Fig. 2 **(a)** Schematic illustration of the preparation of Fe-$NiCo_2O_4$. SEM images of **(b)(c)** NiCo, **(d)(e)** Fe^{2+}-$NiCo_2O_4$, and **(f)(g)** Fe^{3+}-$NiCo_2O_4$.

stacked ultrathin nanosheets. The thickness of nanosheets in the Fe-$NiCo_2O_4$ nanosphere was less than 10 nm. Figure 3(b) shows the rich porous structure in Fe-$NiCo_2O_4$ with rich edges, which was obviously different from the non-characteristic morphology of the undoped iron nitrate sample. These nanosheets were separated and grown in a staggered manner on the sphere frame to form a nanosphere shape with a large number of open spaces. This provided a convenient channel for ion transmission and shortened the diffusion path, which effectively improved the transmission efficiency of ions. Ultrathin nanosheets increased the density of electrochemically active sites and the accessibility of electrolytes, thereby improving the electrocatalyst OER activity. Based on the advanced porous structure with abundant edge sites and compositional advantages, a representative Fe^{3+}-$NiCo_2O_4$ doped with ferric nitrate was selected to study the correlation between composition/structure and catalytic performance of the OER. Figure 3(c) is a typical HRTEM image of the underside of the nanosheet. It was found that many edge defects were distributed on the surface of the nanosheet. The lattice fringes in the corresponding HRTEM image indicate the crystalline nature of nanosheets. The lattice distance marked in the illustration in Fig. 3(d) is approximately 0.245 nm, which corresponds to the (3 1 1) crystal plane of $NiCo_2O_4$.

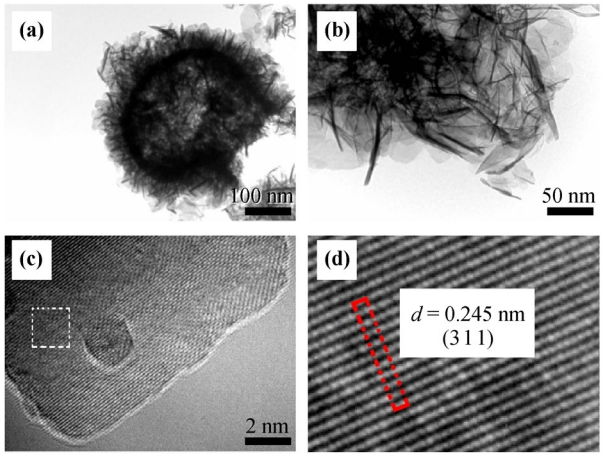

Fig. 3 Structural characterization of Fe^{3+}-$NiCo_2O_4$ hierarchical sphere: **(a)(b)** TEM images; **(c)** HRTEM image; **(d)** image of White Box in the dotted square area in panel (c).

To gain insight into the strong electronic interactions caused by the evolution of composition and structure during the ion-exchange etching, the XPS spectra of $NiCo_2O_4$ and Fe^{3+}-$NiCo_2O_4$ mixed catalysts were compared. The XPS measurement spectrum showed the presences of Ni, Co, Fe and O in the porous Fe^{3+}-$NiCo_2O_4$ nanospheres, which was consistent with the EDX results. The Ni 2p XPS spectrum of the Fe^{3+}-$NiCo_2O_4$ catalyst is presented in Fig. 4(a), while those of the $NiCo_2O_4$ and Fe^{2+}-$NiCo_2O_4$ catalysts are revealed in Figs. S3(a) and S4(a), respectively. In the Ni 2p region of the $NiCo_2O_4$ catalyst, the binding energies of approximately 854.8 and 872.4 eV could be assigned to Ni^{2+}. In the Ni 2p region of the Fe^{3+}-$NiCo_2O_4$ catalyst, the binding energies of approximately 856.1 and 873.9 eV could be attributed to Ni^{3+}, and the satellite peaks centered at 862.0 and 880.1 eV included Ni^{2+} and Ni^{3+} satellites. Compared with the $NiCo_2O_4$ catalyst, the Fe^{3+}-$NiCo_2O_4$ catalyst had different Ni species, and their peak positions had moved about 1.3 eV to the higher binding energy, which means that there was some electron transfer between Fe and Ni after the Fe^{3+} doping [27]. In the Ni 2p region of the Fe^{2+}-$NiCo_2O_4$ catalyst, the binding energies of about 855.3 and 873 eV can be assigned to Ni^{2+}, and are between those of the $NiCo_2O_4$ and Fe^{3+}-$NiCo_2O_4$ catalysts.

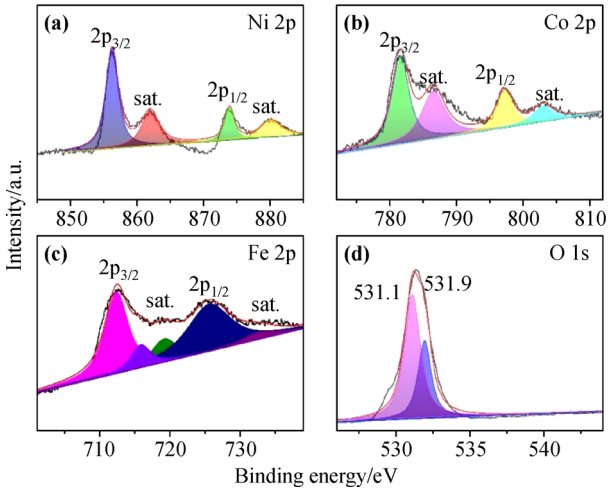

Fig. 4 **(a)** Ni 2p, **(b)** Co 2p, **(c)** Fe 2p, and **(d)** O 1s XPS spectra of samples.

Figure 4(b) shows the high-resolution XPS spectrum of Co 2p of the Fe^{3+}-$NiCo_2O_4$ catalyst. Co 2p for $NiCo_2O_4$ is shown in Fig. S3(b), while Co 2p for Fe^{2+}-$NiCo_2O_4$ is listed in Fig. S4(b). In the Co 2p region of the $NiCo_2O_4$ catalyst, the peaks at 780.4 and the satellite peak at 784.8 eV are obvious in the Co $2p_{3/2}$ region, while the two peaks at 796.2 and the satellite peak at 801.3 eV are in the Co $2p_{1/2}$ region [28–29]. Compared with the $NiCo_2O_4$ catalyst, the Fe^{3+}-$NiCo_2O_4$ catalyst possessed different Co species, and their main peak positions had moved about 1 eV to a higher binding energy, which could be attributed

to the characteristics of Co^{3+}. For the Fe^{2+}-$NiCo_2O_4$ catalyst, the Co $2p_{3/2}$ main peak position was same as for the $NiCo_2O_4$ catalyst (780.4 eV), but the Co $2p_{1/2}$ main peak position had moved about 1 eV (785.2 eV) to the lower binding energy, which could be attributed to the characteristics of Co^{2+}.

Figure 4(c) shows the high-resolution XPS spectrum of Fe 2p of the Fe^{3+}-$NiCo_2O_4$ catalyst. The signals at 712.3 and 715.7 eV can be attributed to Fe^{2+}, and the signals at 719 and 725.1 eV indicate that the Fe atoms can be assigned to Fe^{3+} [30]. Fe 2p for the Fe^{2+}-$NiCo_2O_4$ catalysts are shown in Fig. S4(c), in which the signals at 711.2 and 719.1 eV can be assigned to Fe^{2+}, and the signals at 725 and 732.2 eV revealed that the Fe atoms could be assigned to Fe^{3+} [30].

Figure 4(d) shows the high-resolution XPS spectrum of the O 1s of the Fe^{3+}-$NiCo_2O_4$ catalyst. The O 1s of $NiCo_2O_4$ is shown in Fig. S4(c), and the O 1s of Fe^{2+}-$NiCo_2O_4$ is shown in Fig. S5(c). In the O 1s region of the $NiCo_2O_4$ catalyst, the signals at 530.4 and 531.2 eV can be assigned to lattice oxygen and hydroxyl groups, respectively [31]. For the Fe^{3+}-$NiCo_2O_4$ catalyst, the 531.1 eV fitting peak could be assigned to adsorbed oxygen or hydroxyl groups, while the other O 1s peak at 531.9 eV is usually associated with the surface hydroxide group (O_2). For the Fe^{2+}-$NiCo_2O_4$ catalyst, the signals at 529.6 and 530.9 eV could be assigned to the metal oxygen bond (O1) and hydroxyl groups, respectively.

The electrocatalytic OER activities of the catalyst were evaluated by LSV between 1.0 and 2.0 V with RHE. Figure 5(a) shows the polarization curves of these catalysts. For Fe^{3+}-$NiCo_2O_4$, the anodic peak of 1.35 V before the OER onset potential could be observed, which is attributed to the Ni^{2+}/Ni^{3+} oxidation. The anodic peak is blue shifted, which was due to the suppression of typical Ni^{2+}/Ni^{3+} oxidation by doping Fe atoms. It could be observed that under the same current density, Fe^{3+}-$NiCo_2O_4$ exhibited the best OER catalytic activity at a current density of 10 $mA \cdot cm^{-2}$; it has only a low overpotential of 210 mV, which is much lower than those of IrO_2 (233 mV), Fe^{2+}-$NiCo_2O_4$ (294 mV), and $NiCo_2O_4$ (330 mV). Furthermore, at η_{OER} = 295 mV, Fe^{3+}-$NiCo_2O_4$ can drive an anode current density of 100 $mA \cdot cm^{-2}$, while that driven by the IrO_2 catalyst is 44 $mA \cdot cm^{-2}$. Fe^{3+}-$NiCo_2O_4$ had a lower overpotential than that of IrO_2 for OER, which indicated that the electrocatalytic performance was greatly improved. This result showed that the transformation of electrons between nickel and iron is good for the catalytic reaction, and the incorporation of iron improved the activity of catalytic oxygen evolution.

The Tafel slope is a key electrochemical parameter, which provides in-depth information about the OER

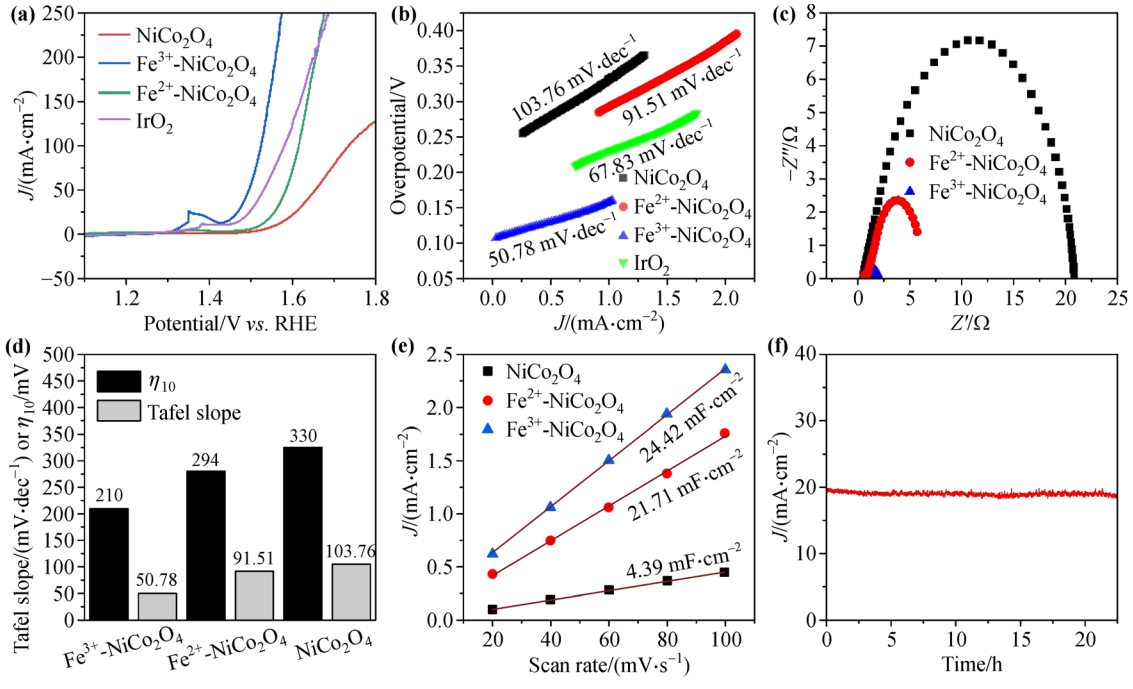

Fig. 5 **(a)** Polarization curves and **(b)** Tafel slopes of $NiCo_2O_4$, Fe^{2+}-$NiCo_2O_4$, Fe^{3+}-$NiCo_2O_4$ and IrO_2 towards OER. **(c)** Nyquist diagrams at 200 mV, **(d)** column diagrams of η_{10} and Tafel slope, and **(e)** electrochemical double-layer capacitances for $NiCo_2O_4$, Fe^{2+}-$NiCo_2O_4$ and Fe^{3+}-$NiCo_2O_4$ catalysts. **(f)** Long-term stability of the Fe^{3+}-$NiCo_2O_4$ catalyst.

mechanism (especially the elucidation of OER dynamics and rate-determining steps). Tafel slopes of the four catalysts are shown in Fig. 5(b). The $NiCo_2O_4$ Tafel slope is 103.76 $mV \cdot dec^{-1}$, while the Fe^{3+}-$NiCo_2O_4$ Tafel slope is 50.78 $mV \cdot dec^{-1}$ which is much smaller than that of the commercial IrO_2 catalyst (67.83 $mV \cdot dec^{-1}$). This indicates that under the same current density, Fe^{3+}-$NiCo_2O_4$ requires the lowest overpotential in catalytic OER reaction, and in a small range of overpotential change, the current density increases faster, which implies good electrocatalytic kinetics. Therefore, the results showed that Fe^{3+}-$NiCo_2O_4$ had a higher OER catalytic rate. Furthermore, electrochemical impedance measurements could be used to analyze the interfacial resistance of the two electrocatalysts (Fig. 5(c)). Fe^{3+}-$NiCo_2O_4$ had a smaller resistance than $NiCo_2O_4$, which also revealed its excellent charge transfer ability during the OER catalysis process.

To further explore the catalytic activity of $NiCo_2O_4$ and Fe-$NiCo_2O_4$ catalysts, we explored the electrochemically active surface area (ECSA) of the catalyst, as the ECSA usually positively correlates with the electrochemical double-layer capacitance (C_{dl}). By conducting the cyclic voltammetry scans of the intervals as shown in Fig. S5, where the redox reaction does not occur, the corresponding C_{dl} was calculated. The $NiCo_2O_4$ C_{dl} value was 4.39 $mF \cdot cm^{-2}$, while the Fe^{3+}-$NiCo_2O_4$ C_{dl} value (24.42 $mF \cdot cm^{-2}$) was relatively higher (Fig. 5(e)), which suggests that Fe^{3+}-$NiCo_2O_4$ had larger ECSA and more active catalytic sites, thus more conducive to the OER catalytic reaction.

In order to understand the influence of Fe doping on the intrinsic OER activity, TOF data of the OER electrocatalyst were obtained by the following equation:

$$\mathrm{TOF} = \frac{J \times A}{4 \times n \times F} \tag{2}$$

where J is the OER current density, A is the surface area of the anode, and F is the Faraday constant. As shown in Fig. S6, under the same overpotential, the TOF of Fe^{3+}-$NiCo_2O_4$ was much higher than that of $NiCo_2O_4$. For instance, when η was 350 mV, the TOF of Fe^{3+}-$NiCo_2O_4$ was 10.63 s^{-1}, 4.80 and 7.19 times those of Fe^{2+}-$NiCo_2O_4$ and $NiCo_2O_4$, respectively. In general, the incorporation of Fe^{3+} could enhance the OER activity of the nanosphere, and changed the OER mechanism at the same time.

To further understand the catalytic mechanism of Fe^{3+}-$NiCo_2O_4$, static contact angle measurements were performed to detect the accessibility of $NiCo_2O_4$, Fe^{2+}-$NiCo_2O_4$ and Fe^{3+}-$NiCo_2O_4$ surface electrolytes. As shown in Fig. S7, Fe^{3+}-$NiCo_2O_4$ could promote water adsorption, and the contact angle was 41.64°, which is smaller than those of Fe^{2+}-$NiCo_2O_4$ (43.45°) and $NiCo_2O_4$ (70.62°), suggesting that the Fe^{3+}-$NiCo_2O_4$ had more oxygen vacancies. The hydrophilic ability was conductive to the adsorption and permeation of electrolyte.

We used the Kubelka–Munk diagram of bandgap energy and ultraviolet–visible (UV–Vis) absorption spectroscopy to analyze the physical mechanism of hybrid atom doping. In Fig. S8, the bandgap energies of $NiCo_2O_4$, Fe^{2+}-$NiCo_2O_4$ and Fe^{3+}-$NiCo_2O_4$ are seen to be 1.3, 1.26 and 1.2 eV, respectively. This means that the bandgap of $NiCo_2O_4$ nanosphere was effectively reduced by introducing hybrid atoms.

The above results achieved with data of Tafel slope, R_{ct}, C_{dl}, TOF, contact angle and bandgap energy showed that the Fe^{3+}-$NiCo_2O_4$ catalyst exhibited obviously improved OER activity compared with the pure $NiCo_2O_4$ nanosphere catalyst (Table S1). Among these catalysts, the highest OER activity appeared by doping with Fe atom. In addition, the Fe^{3+}-$NiCo_2O_4$ nanospheres had outstanding performance which was evenly matched with advanced OER catalysts as recently reported [32–41], due to the fact that both Ni and Co were changed from 2 + to 3 + upon the Fe^{3+} doping. Thus, in order to further evaluate which species have a major effect on the OER, we prepared Fe^{3+}-NiO and Fe^{3+}-CoO nanosphere catalysts. The polarization curves illustrate that the Fe^{3+}-NiO catalyst exhibited considerably higher OER activity than that of Fe^{3+}-CoO (Fig. S9). For example, the Fe^{3+}-NiO catalyst could drive a current density of 10 $mA \cdot cm^{-2}$ at 240 mV, while the Fe^{3+}-CoO catalyst required an overpotential of 327 mV. The above results indicate that the Fe^{3+}-CoO species in the Fe^{3+}-$NiCo_2O_4$ nanosphere is the inactive one in OER.

The comparison of the catalytic activities of OER on Fe^{3+}-$NiCo_2O_4$ with recently reported catalysts is summarized in Table 1 [7–8,11–12,14–16,22,25–26,32–37].

Moreover, stability is another unignorable factor behind the bulk water electrolysis of the catalyst. Under a given overpotential (1.46 V), the long-term durability of the catalyst was further tested in the bulk electrolysis of water. Figure 5(f) shows that some current drops existed when the potentiostatic measurement started, and afterwards the anode current density showed that the catalyst had subtle

Table 1 Comparison of the catalytic activities of OER on Fe^{3+}-$NiCo_2O_4$ with recently reported catalysts in the 1.0 mol·L^{-1} KOH medium (pH = 14)

Catalyst	η/mV *vs.* RHE	Ref.
Fe^{3+}-$NiCo_2O_4$	210	this work
Fe^{2+}-$NiCo_2O_4$	294	this work
$NiCo_2O_4$	330	this work
$A_{0.25}$B-NiFe	237	[7]
Ni/Ni(OH)$_2$	310	[8]
CF@NiP_x	200	[11]
d-$NiC_{0.2}$NS/Ni/CF	228	[12]
CoS_2@HADC	226	[14]
Fe-$NiCo_2O_4$	265	[15]
$NiCo_2O_4$/NF	310	[16]
C-doped Co/Co_3O_4	352	[22]
Fe-$NiMoO_4$	217	[25]
Ni–Fe–S	223	[26]
CoCu-ZIF@GDY	250	[32]
Ni_4Cu_2@C	280	[33]
ECT-S-$Co_{0.37}Ni_{0.26}Fe_{0.37}O$	232	[34]
$FeNi_3$N-h	210	[35]
CoCuNCNT@PC-700-2	340	[36]
Co–Fe–P–Se	270	[37]

Note: η is the overpotential measured at 10 mA·cm^{-2}.

degradation within 22 h. After 22 h of potentiostatic measurement, the current density was still 21 mA·cm^{-2} at an overpotential of 230 mV, further proving the robust stability of the Fe^{3+}-$NiCo_2O_4$ nanosphere catalyst in a strong alkaline electrolyte. The current density driven by the Fe^{2+}-$NiCo_2O_4$ pair at 1.58 V dramatically decreased from 50 to about 20 mA·cm^{-2} after 7 h (Fig. S10). The structure of the Fe^{3+}-$NiCo_2O_4$ nanosphere catalyst after the OER process at η_{OER} = 210 mV for 1 h was characterized by SEM and XPS. The SEM image shows that the Fe^{3+}-$NiCo_2O_4$ nanospheres remain almost intact in morphology (Fig. S11). The surface valence states of the Fe^{3+}-$NiCo_2O_4$ nanosphere catalyst before and after the OER process were obviously different. As shown in Fig. S12(a), in the Ni 2p region of the Fe^{3+}-$NiCo_2O_4$ catalyst after the OER process, there were binding energies of approximately 854.4 and 873.6 eV, and the satellite peaks centered at 859.1 and 879.1 eV could be attributed to Ni^{2+} [27]. It was found that the peaks of Ni^{3+} disappeared after the OER process. As shown in Fig. S12(b), in the Co 2p region of the Fe^{3+}-$NiCo_2O_4$ catalyst after the OER process, the positions of peaks were different from the Fe^{3+}-$NiCo_2O_4$ nanosphere catalyst before the OER process, and the peaks of Co^{3+} disappeared after the OER process [28–29]. As shown in Fig. S12(c), in the Fe 2p region of the Fe^{3+}-$NiCo_2O_4$ catalyst after the OER process, the signal at 707 eV could be attributed to Fe^{3+}-NiO; the signal at 710.8 eV could be attributed to Fe_2O_3; and the signals at 715 and 725 eV could be assigned to FeOOH [30]. The XPS results of the Fe^{3+}-$NiCo_2O_4$ catalyst after the OER process indicated that the Fe atom was the active center of the Fe^{3+}-$NiCo_2O_4$ catalyst. The good catalytic activity and long-term stability indicates that Fe^{3+}-$NiCo_2O_4$ nanospheres can be used as high-activity catalysts for OER in alkaline media with price advantage.

4 Conclusions

In summary, we designed and synthesized Fe-doped nanospheres with hollow porous structure by a Fe^{3+}-$NiCo_2O_4$ simple solvothermal ion exchange method. Compared with the $NiCo_2O_4$ catalyst, the Fe^{3+}-$NiCo_2O_4$ catalyst possesses different Ni and Co species, and their XPS peak positions move to a higher binding energy, which means that there is partial electron transfer between Fe and NiCo after the Fe^{3+} doping. Ni and Co transfer from 2+ to 3+ after the Fe^{3+} doping. The Fe atom-doped $NiCo_2O_4$ nanosphere catalyst exhibits significantly enhanced OER activity which is better than most reported catalysts, including the pure $NiCo_2O_4$ nanosphere catalyst. When driving a current density of 10 mA·cm^{-2}, the Fe^{3+}-$NiCo_2O_4$ nanosphere catalyst can act under an overpotential of 210 mV. In addition, the Fe^{3+}-$NiCo_2O_4$ nanosphere catalyst also has outstanding long-term stability. The excellent activity and long-term stability give the Fe^{3+}-$NiCo_2O_4$ nanosphere catalyst broad application potential in large-scale water splitting.

Disclosure of potential conflicts of interests The authors declare no competing financial interest.

Acknowledgements This work was supported by the Department of Education Basic Research Operating Costs of Heilongjiang Province, China (Grant No. 135309353).

References

[1] Aricò A S, Bruce P, Scrosati B, et al. Nanostructured materials for advanced energy conversion and storage devices. Nature Materials, 2005, 4(5): 366–377

[2] Gray H B. Powering the planet with solar fuel. Nature Chemistry, 2009, 1(1): 7

[3] Cook T R, Dogutan D K, Reece S Y, et al. Solar energy supply and storage for the legacy and nonlegacy worlds. Chemical Reviews, 2010, 110(11): 6474–6502

[4] Zhao Y, Nakamura R, Kamiya K, et al. Nitrogen-doped carbon nanomaterials as non-metal electrocatalysts for water oxidation. Nature Communications, 2013, 4(1): 2390

[5] You B, Sun Y. Innovative strategies for electrocatalytic water splitting. Accounts of Chemical Research, 2018, 51(7): 1571–1580

[6] Poulain R, Klein A, Proost J. Electrocatalytic properties of (1 0 0)-, (1 1 0)-, and (1 1 1)-oriented NiO thin films toward the oxygen evolution reaction. The Journal of Physical Chemistry C, 2018, 122(39): 22252–22263

[7] Pan S, Kong X, Zhang Q, et al. Rational modulating electronegativity of substituents in amorphous metal-organic frameworks for water oxidation catalysis. International Journal of Hydrogen Energy, 2020, 45(16): 9723–9732

[8] Lim D W, Kim S J, Kim N, et al. Strongly coupled $Ni/Ni(OH)_2$ hybrid nanocomposites as highly active bifunctional electrocatalysts for overall water splitting. ACS Sustainable Chemistry & Engineering, 2020, 8(11): 4431–4439

[9] Jing F, Lv Q Y, Xiao J, et al. Highly active and dual-function self-supported multiphase $NiS–NiS_2–Ni_3S_2$/NF electrodes for overall water splitting. Journal of Materials Chemistry A: Materials for Energy and Sustainability, 2018, 6(29): 14207–14214

[10] Li Q, Wang D W, Han C, et al. Construction of amorphous interface in an interwoven NiS/NiS_2 structure for enhanced overall water splitting. Journal of Materials Chemistry A: Materials for Energy and Sustainability, 2018, 6(18): 8233–8237

[11] Zhang Z Y, Liu S S, Xiao J, et al. Fiber-based multifunctional nickel phosphide electrodes for flexible energy conversion and storage. Journal of Materials Chemistry A: Materials for Energy and Sustainability, 2016, 4(24): 9691–9699

[12] Yang H D, Luo S, Li X Z, et al. Controllable orientation-dependent crystal growth of high-index faceted dendritic $NiC_{0.2}$ nanosheets as high-performance bifunctional electrocatalysts for overall water splitting. Journal of Materials Chemistry A: Materials for Energy and Sustainability, 2016, 4(47): 18499–18508

[13] Ray C T, Lee S C, Jin B J, et al. Conceptual design of three-dimensional CoN/Ni_3N-coupled nanograsses integrated on N-doped carbon to serve as efficient and robust water splitting electrocatalysts. Journal of Materials Chemistry A: Materials for Energy and Sustainability, 2018, 6(10): 4466–4476

[14] Li B, Xing R, Mohite S V, et al. CoS_2 nanodots anchored into heteroatom-doped carbon layer via a biomimetic strategy: Boosting the oxygen evolution and supercapacitor performance. Journal of Power Sources, 2019, 436: 226862

[15] Wei P, Yang Y, Kang H, et al. Controllable synthesis of Fe-doped $NiCo_2O_4$ nanobelts as superior catalysts for oxygen evolution reaction. Chemistry: A European Journal, 2020, 26(60): 13725–13729

[16] Dymerska A, Kukułka W, Biegun M, et al. Spinel of nickel–cobalt oxide with rod-like architecture as electrocatalyst for oxygen evolution reaction. Materials, 2020, 13(18): 3918

[17] Jiang Z, Jiang Z J, Maiyalagan T, et al. Cobalt oxide-coated N- and B-doped graphene hollow spheres as bifunctional electrocatalysts for oxygen reduction and oxygen evolution reactions. Journal of Materials Chemistry A: Materials for Energy and Sustainability, 2016, 4(16): 5877–5889

[18] Chen S, Cheng J, Ma L, et al. Light-weight 3D Co–N-doped hollow carbon spheres as efficient electrocatalysts for rechargeable zinc–air batteries. Nanoscale, 2018, 10(22): 10412–10419

[19] Zeng L Y, Sun K, Chen Y J, et al. Neutral-pH overall water splitting catalyzed efficiently by a hollow and porous structured ternary nickel sulfoselenide electrocatalyst. Journal of Materials Chemistry A: Materials for Energy and Sustainability, 2019, 7 (28): 16793–16802

[20] Diao L C, Qin J, Zhao N Q, et al. "Ethanol–water exchange" nanobubbles templated hierarchical hollow β-Mo_2C/N-doped carbon composite nanospheres as an efficient hydrogen evolution electrocatalyst. Journal of Materials Chemistry A: Materials for Energy and Sustainability, 2018, 6(14): 6054–6064

[21] Ma R G, Xing R H, Lin G X, et al. Graphene-wrapped nitrogen-doped hollow carbon spheres for high-activity oxygen electroreduction. Materials Chemistry Frontiers, 2018, 2(8): 1489–1497

[22] Hang L F, Sun Y Q, Men D D, et al. Hierarchical micro/nanostructured C doped Co/Co_3O_4 hollow spheres derived from $PS@Co(OH)_2$ for the oxygen evolution reaction. Journal of Materials Chemistry A: Materials for Energy and Sustainability, 2017, 5(22): 11163–11170

[23] Friebel D, Louie M W, Bajdich M, et al. Identification of highly active Fe sites in (Ni,Fe)OOH for electrocatalytic water splitting. Journal of the American Chemical Society, 2015, 137(3): 1305–1313

[24] Burke M S, Kast M G, Trotochaud L, et al. Cobalt–iron (oxy)-hydroxide oxygen evolution electrocatalysts: The role of structure and composition on activity, stability, and mechanism. Journal of the American Chemical Society, 2015, 137(10): 3638–3648

[25] Yin Z X, Zhang S, Chen W, et al. Hybrid-atom-doped $NiMoO_4$ nanotubes for oxygen evolution reaction. New Journal of Chemistry, 2020, 44(40): 17477–17482

[26] Yin Z X, Zhang S, Li J L, et al. *In-situ* fabrication of Ni–Fe–S hollow hierarchical sphere: An efficient (pre)catalyst for OER and HER. New Journal of Chemistry, 2021, 45(29): 12996–13003

[27] Marco J F, Gancedo J R, Gracia M, et al. Characterization of the nickel cobaltite, $NiCo_2O_4$, prepared by several methods: An XRD, XANES, EXAFS, and XPS study. Journal of Solid State Chemistry, 2000, 153(1): 74–81

[28] Kim J G, Pugmire D L, Battaglia D, et al. Analysis of the $NiCo_2O_4$

spinel surface with Auger and X-ray photoelectron spectroscopy. Applied Surface Science, 2000, 165(1): 70–84

[29] Jin C, Lu F L, Cao X C, et al. Facile synthesis and excellent electrochemical properties of $NiCo_2O_4$ spinel nanowire arrays as a bifunctional catalyst for the oxygen reduction and evolution reaction. Journal of Materials Chemistry A: Materials for Energy and Sustainability, 2013, 1(39): 12170–12177

[30] Yamashita T, Hayes P. Analysis of XPS spectra of Fe^{2+} and Fe^{3+} ions in oxide materials. Applied Surface Science, 2008, 254(8): 2441–2449

[31] Biesinger M C, Payne B P, Grosvenor A P, et al. Resolving surface chemical states in XPS analysis of first row transition metals, oxides and hydroxides: Cr, Mn, Fe, Co and Ni. Applied Surface Science, 2011, 257(7): 2717–2730

[32] Cui J, Liu J M, Wang C B, et al. Efficient electrocatalytic water oxidation by using the hierarchical 1D/2D structural nanohybrid of CoCu-based zeolitic imidazolate framework nanosheets and graphdiyne nanowires. Electrochimica Acta, 2020, 334(1): 135577

[33] Lin L, Chen M, Wu L. Facile synthesis of nickel–copper hollow spheres as efficient bifunctional electrocatalysts for overall water splitting. Materials Chemistry Frontiers, 2020, 4(3): 996–1005

[34] Chen W, Liu Y, Li Y, et al. *In-situ* electrochemically derived nanoporous oxides from transition metal dichalcogenides for active oxygen evolution catalysts. Nano Letters, 2016, 16(12): 7588–7596

[35] Liu Z, Liu D, Zhao L, et al. Efficient overall water splitting catalyzed by robust $FeNi_3N$ nanoparticles with hollow interiors. Journal of Materials Chemistry A, 2021, 9(12): 7750–7758

[36] Liu G P, Wang B, Ding P H, et al. *In-situ* synthesis strategy for CoM (M = Fe, Ni, Cu) bimetallic nanoparticles decorated N-doped 1D carbon nanotubes/3D porous carbon for electrocatalytic oxygen evolution reaction. Journal of Alloys and Compounds, 2020, 815: 152470

[37] Wu H, Wang J, Yan J, et al. MOF-derived two-dimensional N-doped carbon nanosheets coupled with Co–Fe–P–Se as efficient bifunctional OER/ORR catalysts. Nanoscale, 2019, 11(42): 20144–20150

[38] Li G, Zhang X, Zhang H, et al. Bottom-up MOF-intermediated synthesis of 3D hierarchical flower-like cobalt-based homobimetallic phophide composed of ultrathin nanosheets for highly efficient oxygen evolution reaction. Applied Catalysis B: Environmental, 2019, 249: 147–154

[39] Budiyanto E, Yu M Q, Chen M M, et al. Tailoring morphology and electronic structure of cobalt iron oxide nanowires for electrochemical oxygen evolution reaction. ACS Applied Energy Materials, 2020, 3(9): 8583–8594

[40] Tang Y J, Zhang A M, Zhu H J, et al. Polyoxometalate precursors for precisely controlled synthesis of bimetallic sulfide heterostructure through nucleation-doping competition. Nanoscale, 2018, 10(18): 8404–8412

[41] Deng X, Öztürk S, Weidenthaler C, et al. Iron-induced activation of ordered mesoporous nickel cobalt oxide electrocatalyst for the oxygen evolution reaction. ACS Applied Materials & Interfaces, 2017, 9(25): 21225–21233

Supplementary information

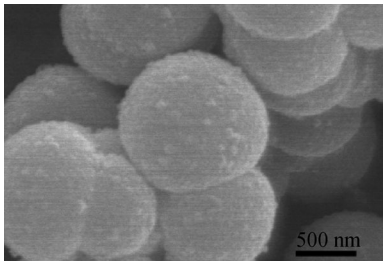

Fig. S1 SEM image of the $NiCo_2O_4$ nanosphere.

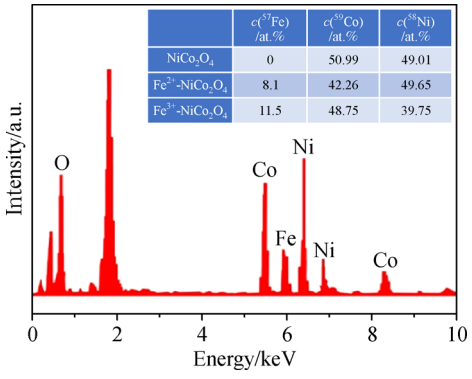

Fig. S2 The half-quantitative SEM-EDX result of Fe^{3+}-$NiCo_2O_4$; the insert shows ICP-OES results of $NiCo_2O_4$, Fe^{2+}-$NiCo_2O_4$ and Fe^{3+}-$NiCo_2O_4$.

Table S1 Detailed parameters of $NiCo_2O_4$, Fe^{2+}-$NiCo_2O_4$, Fe^{3+}-$NiCo_2O_4$ and IrO_2 towards OER

Material	η/mV [a]	E/V [b]	$R_{ct}/(\Omega\cdot cm^2)$	$C_{dl}/(mF\cdot cm^{-2})$	TOF/s^{-1} [d]
$NiCo_2O_4$	330	1.41 [c]	1.4	4.39	1.478
Fe^{2+}-$NiCo_2O_4$	294	–	1.7	21.71	2.216
Fe^{3+}-$NiCo_2O_4$	210	–	1.3	24.42	10.63
IrO_2	233	–	–	–	–

a) η is the overpotential *vs.* RHE measured at 10 $mA\cdot cm^{-2}$. b) Potential corresponding to the anodic peak position. c) This value is versus RHE. d) At 350 mV.

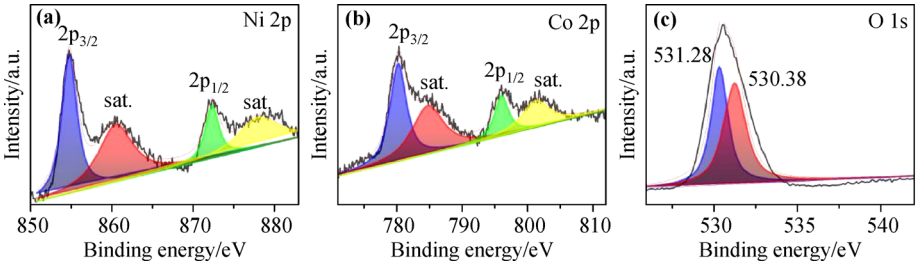

Fig. S3 **(a)** Ni 2p, **(b)** Co 2p, and **(c)** O 1s XPS spectra of $NiCo_2O_4$.

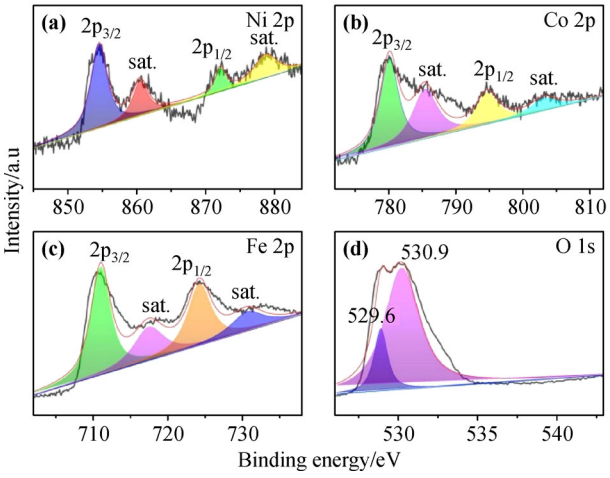

Fig. S4 **(a)** Ni 2p, **(b)** Co 2p, **(c)** Fe 2p, and **(d)** O 1s XPS spectra of Fe^{2+}-$NiCo_2O_4$.

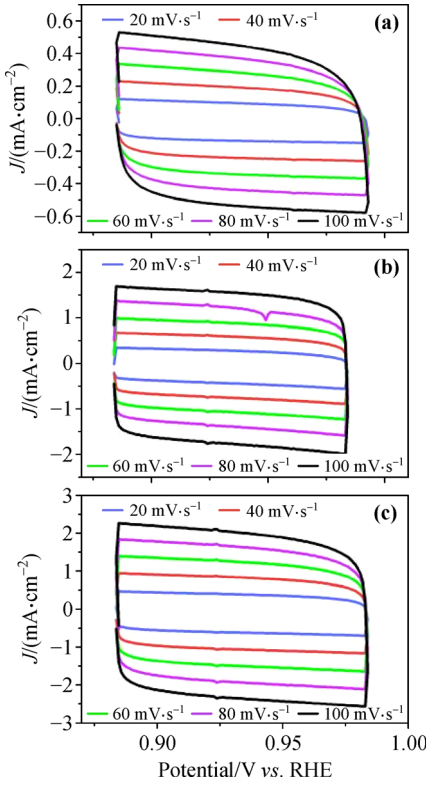

Fig. S5 Cyclic voltammograms of **(a)** $NiCo_2O_4$, **(b)** Fe^{2+}-$NiCo_2O_4$, and **(c)** Fe^{3+}-$NiCo_2O_4$.

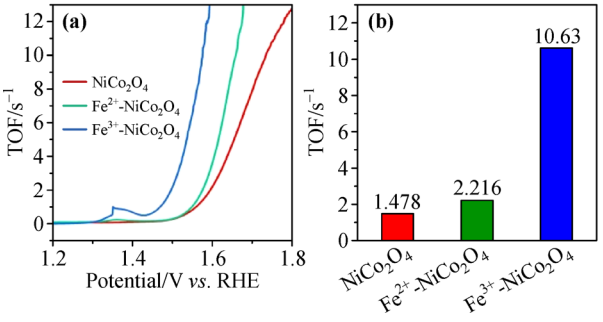

Fig. S6 **(a)** TOF versus potential curves and **(b)** TOF values at 350 mV of $NiCo_2O_4$, Fe^{2+}-$NiCo_2O_4$, and Fe^{3+}-$NiCo_2O_4$.

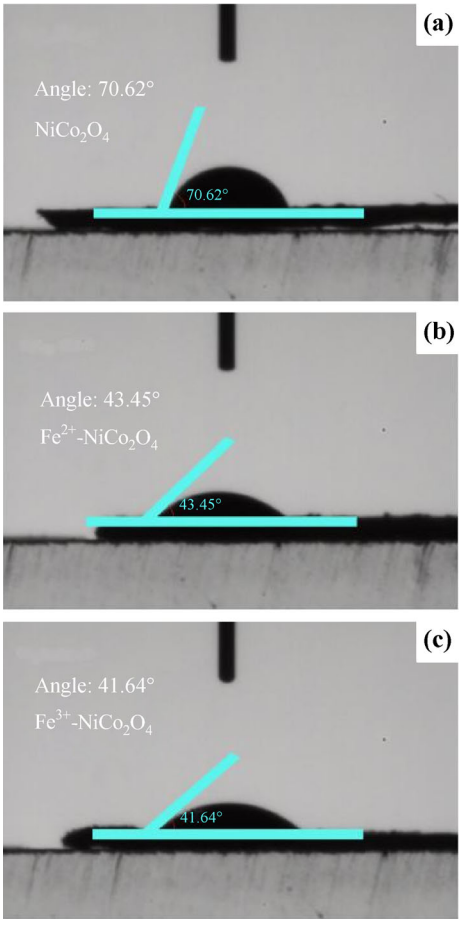

Fig. S7 Contact angles of **(a)** $NiCo_2O_4$, **(b)** Fe^{2+}-$NiCo_2O_4$, and **(c)** Fe^{3+}-$NiCo_2O_4$.

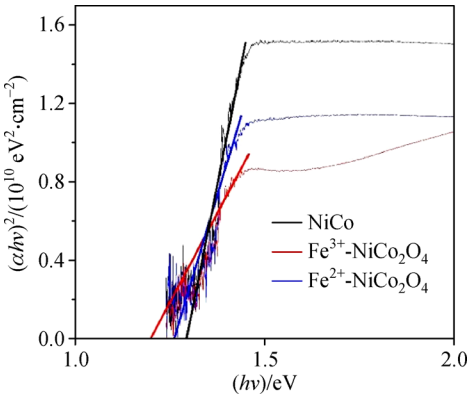

Fig. S8 Kubelka–Munk plots for bandgap energies of $NiCo_2O_4$, Fe^{2+}-$NiCo_2O_4$, and Fe^{3+}-$NiCo_2O_4$.

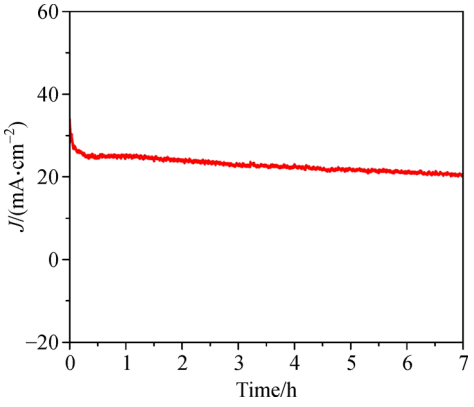

Fig. S10 The time-dependent current density curve of Fe^{2+}-$NiCo_2O_4$ at a current density of 50 $mA \cdot cm^{-2}$ in the 1.0 $mol \cdot L^{-1}$ KOH solution.

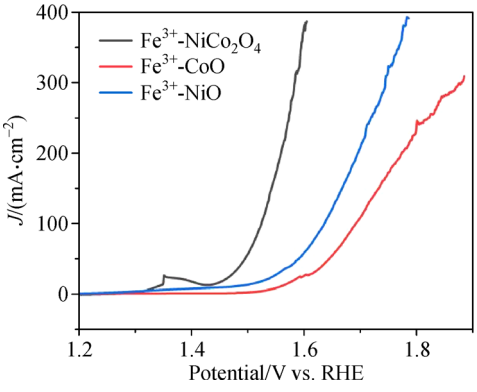

Fig. S9 Polarization curves of Fe^{3+}-$NiCo_2O_4$, Fe^{3+}-CoO and Fe^{3+}-NiO.

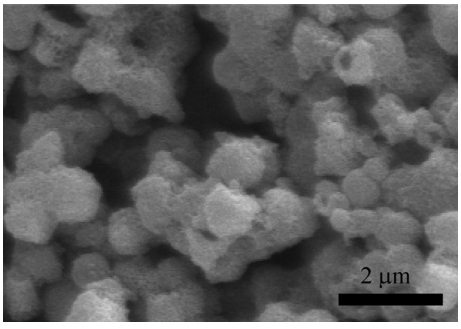

Fig. S11 SEM image of the Fe^{3+}-$NiCo_2O_4$ nanosphere catalyst after the OER process.

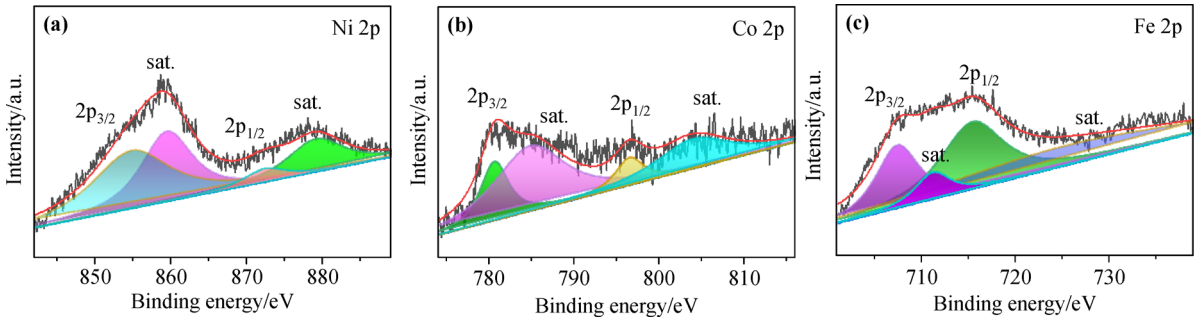

Fig. S12 **(a)** Ni 2p, **(b)** Co 2p, and **(c)** Fe 2p XPS spectra of the Fe^{3+}-$NiCo_2O_4$ nanosphere catalyst after OER.